Dalton Transactions

Accepted Manuscript

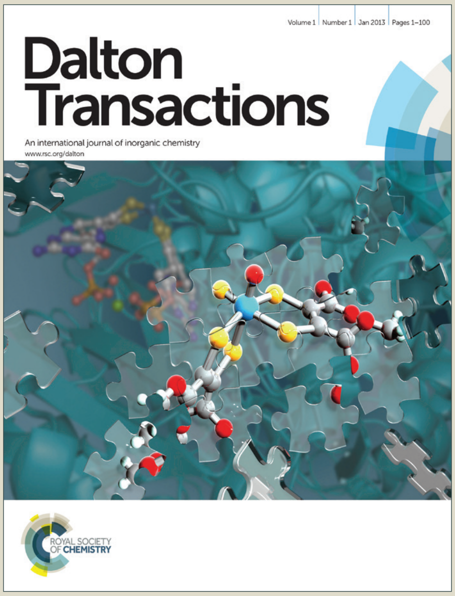

Volume 1 | Number 1 | Jan 2013 | Pages 1–100

Dalton Transactions

An international journal of inorganic chemistry

www.rsc.org/dalton

ROYAL SOCIETY
OF CHEMISTRY

www.rsc.org/dalton

Journal Name RSCPublishing

ARTICLE

Cite this: DOI: 10.1039/x0xx00000x

Oxidation of Methane by an N-bridged High-Valent Diiron-Oxo Species: Electronic Structure Implications to the Reactivity

Mursaleem Ansari, Nidhi Vyas, Azaj Ansari and Gopalan Rajaraman[†*]

Received 00th January 2012,
Accepted 00th January 2012

DOI: 10.1039/x0xx00000x

www.rsc.org/

High-valent iron-oxo species are key intermediates in C-H bond activation of several substrates including alkanes. The biomimic heme and non-heme mononuclear Fe(IV)=O complexes are very popular in this area and has been thoroughly studied over the years. These species despite possessing aggressive catalytic abilities, cannot easily activate inert C-H bonds such as those of methane. In this context dinuclear complexes have gained attention, particularly μ-nitrido dinuclear iron species $[(TPP)(m\text{-}CBA)Fe(IV)(\mu\text{-}N)Fe(IV)(O)(TPP^{\bullet+})]^-$ reported lately exhibit remarkable catalytic abilities towards substrates such as methane. Here using DFT methods, we have explored the electronic structure and complex spin-state energetics present in this species. To gain insights in to the nature of bonding, we have computed the absorption, the EPR and the Mössbauer parameters and have probed the mechanism of methane oxidation by the dinuclear Fe(IV)=O species. Calculated results are in agreement with the experimental data and our calculations predicts that in $[(TPP)(m\text{-}CBA)Fe(IV)(\mu\text{-}N)Fe(IV)(O)(TPP^{\bullet+})]^-$ species, the two high-spin iron centres are antiferromagnetically coupled leading to a doublet ground state. Our calculations estimate an extremely low kinetic barrier of 26.6 kJ/mol (at doublet surface) for the C-H bond activation of methane by the dinuclear Fe(IV)=O species. Besides this mechanistic studies on the methane activation reveal the unique electronic cooperativity present in this type of dinuclear complexes and unravel the key question on why mononuclear analogues are unable to perform such reactions.

Introduction

Selective oxidation of the thermodynamically strong and kinetically inert C–H bonds of hydrocarbon has been a subject of intensive study for the development of economical and sustainable global carbon management in the pursuit of alternating fuels, in particular methane to methanol conversion.[1-3] A wide range of important chemical and biological reactions occur at high-valent metal centres embedded in the active sites of metalloenzymes such as Methane monooxygenese (sMMO), cytochrome P450, Cytochrome c peroxidases.[4-7] The function of these metalloenzymes and their significance has inspired numerous studies in the synthesis of model complexes mimicking the mechanism of these remarkable catalytic reactions.[8-11] These efforts investigate ways to enhance efficiency and selectivity at will, as well as provide important tools for understanding these enzymatic processes.[12-15] Over the past decades large body of literatures are available on non-heme Fe(IV)=O complexes using the polydentate chelating ligand such as TPA (tris(2-pyridylmethyl)amine), TMC (1,4,7,10-tetramethyl-1,4,7,10-tetraazacyclododecane), bispidines,[16-21] Salen, Corrole and Porphyrin.[22-27] Both mono and dinuclear oxo complexes are explored in this area, however, the μ-oxo dimers are not completely stable under catalytic conditions and often decomposes resulting in a decrease of selectivity of the oxidation process. The nitrogen bridged bimetallic systems possessing particularly the macrocyclic ligands are fascinating as they are very robust and are stable compared to the μ-oxo analogues.[28] Ercolani and co-workers have reported[29-35] several dinuclear complexes such as $[(TPP)Fe]_2N$ (TPP= tetraphenylporphyrin) and $[(Pc)Fe]_2N$ (Pc= phthalocyanine) and thoroughly characterized them using spectroscopic methods. Further progress has been made by Sorokin and co-workers in the preparation and characterization of a series of μ-nitrido bridged diiron phthalocyanines and its substituted complexes. With the aim to probe the electronic structure and nature of the species involved in the catalytic cycles[36-41] these complexes are characterized thoroughly using EPR, absorption, Mössbauer, XANES and EXAFS techniques. Recently, X-ray absorption and emission spectroscopy, along with theoretical calculations on the Fe−X−Fe (X= C, N, O) core were investigated by

Sorokin *et al*. revealing superiority of nitrogen bridged complexes over oxo analogues for oxidation reactions.[42] Theoretical calculations on this set of complexes were recently performed to analyse the electronic structure and their catalytic potential.[43]

Notably Sorokin *et al*. has synthesised [(TPP)(*m*-CBA)Fe(IV)(μ-N)Fe(IV)(O)(TPP$^{\bullet+}$)]$^-$ dinuclear species and characterized them using EPR, UV/Vis and Mössbauer techniques. Examination of its catalytic ability reveals that these species can oxidize variety of alkanes including the most difficult ones such as methane.[41] Apart from the experimental studies, quantum chemical calculations were also extensively used in this area to gain insights into the electronic structure of the catalytically active species and to explore the mechanism of the catalytic reactions.[44-46] Particularly the potency of the nitride bridge over O^{2-} bridge on their catalytic abilities has been rationalized earlier using DFT calculations.[43, 47] Recently our group has reported comparative oxidative abilities of Fe(IV)=NTs with Fe(IV)=O species and also explored the mechanism of *ortho*-hydroxylation of aromatic acids by an Fe(V)=O oxidant.[48, 49] Although there are several reports on the electronic structure and mechanistic studies of mononuclear high-valent iron-oxo species, studies on dinuclear iron-oxo species are rare due to the presence of several spin states arising from the exchange coupling between the two metal centres and are often challenging to compute all these spin states in dinuclear species.[43, 47, 50, 51] In this regard, the report of [(TPP)(*m*-CBA)Fe(IV)(μ-N)Fe(IV)(O)(TPP$^{\bullet+}$)]$^-$ tetraphenylporphyrin cation radical species gained our attention as it possesses both nitrido and oxo group which are reported to have diverse reactivity patterns.[41] In this manuscript we aim to perform density functional theory calculations on *N*-bridged non-heme dimer [(TPP)Fe(III)(μ-N)Fe(IV)(TPP)] in the formation of an oxo–diiron(IV) porphyrin cation radical complex and explore its reactivity for oxidation of methane. With this study, we aim to answer the following intriguing questions, (1) What is nature of bonding in μ-nitrido dinuclear Fe species and what are the energetics of formation for the diiron(IV) analogues? (2) What is the nature of the ground state in these species and how does the calculation of ground state spectroscopic parameters (EPR, absorption and Mössbauer) compare with that of the experiments? (3) What are the mechanistic pathways by which the diiron(IV) activates the C-H bond of methane and what is the origin for its very high reactivity?

Computational Details

All calculations were performed using the Gaussian 09 suite of programs on model complex of TPP ligand where the bulky phenyl groups are modelled as H -atom.[52] The EPR, UV/Vis and Mössbauer spectral parameters of the species were computed using ORCA 2.9 software suite incorporating COSMO solvation effects.[53] The geometries were optimized using the B3LYP-D2 functional, incorporating the dispersion correction proposed by Grimme *et al*.[54] This functional has been employed by us and others earlier to predict correct spin state energetic of several mononuclear metal-oxo/hydroxo/superoxo complexes.[49, 55] Two different basis sets were used; LanL2DZ, which encompasses a double-ζ quality basis set with the Los Alamos effective core potential for Fe and a 6–31G basis set for the other atoms (C, H, N, O and Cl).[56-58] A single point calculation was performed using TZVP basis set for all the atoms.[59, 60] Frequency calculation on the optimized structures were undertaken to confirm the minima on the potential-energy surface (PES) and also to obtain zero-point energy corrections. The quoted DFT energies are B3LYP-D2 solvation energy including free-energy corrections from the frequency calculations at the temperature of 298.15 K. The transitions states were characterized by single negative frequency which pertains to the desired motion as visualized in Chemcraft.[61] The role of solvation on the structures and energetics was studied at the B3LYP-D2 level using the polarizable continuum solvent (PCM) model using acetonitrile as the solvent.[62] The *J* values were computed from the energy differences between the high spin (E_{HS}) state calculated using single determinant wave functions, and the low spin (E_{BS}) state determined using the Broken Symmetry (BS) approach developed by Noodleman.[63, 64] Negative and positive values for *J* correspond to antiferromagnetic and ferromagnetic interactions respectively. Elaborate discussion of the computational methodology employed to compute the exchange interaction is discussed in detail elsewhere.[65] The following notation $^{M}\mathbf{1}_{(sFe1,sFe2)}$ where superscript 'M' denotes the total multiplicities of the spin-coupled dimer and subscript '$_{(sFe1,sFe2)}$' denotes the spin multiplicity on Fe(1) and Fe(2) atoms are employed throughout the manuscript. All spectroscopic parameters calculation incorporate relativistic effect via zeroth-order regular approximation method (ZORA) as implemented in ORCA suite.[66, 67] The MB-Isomer shifts (IS) were calculated based on the calibration constants reported by Römelt *et al*. and 0.16 barn was used for the calculation of quadruple moment of ^{57}Fe nuclei.[68] Calculation of g-anisotropy incorporates spin-orbit coupling using mean-field approximation and this methodology has been widely employed to compute the g-anisotropy.[69] Time dependent density functional theory (TD-DFT) implemented in the ORCA program was used for the calculation of excitation energies. MO and NBO analysis were performed using G09 suite and visualization are done using Chemcraft software.

Results and Discussion

Electronic structure of μ-nitrido dinuclear iron species:

Sorokin and co-workers reported a dinuclear [(TPP)Fe(III)(μ-N)Fe(IV)(TPP)](**1**) as a starting point which upon reaction with *m*-CPBA (*m*-CPBA= meta-chloroperbenzoic acid) yields *m*-CPBA coordinated [(TPP)(*m*-CPBA)Fe(III)(μ-N)Fe(IV)(TPP)] (**1a**) species. Species **1a** undergoes heterolytic cleavage of the O-O bond of the *m*-CPBA leading to the formation of the catalytically active [(TPP)(*m*-CBA)Fe(IV)(μ-N)Fe(IV)(O)(TPP$^{\bullet+}$)]$^-$ (**2**) species (see Scheme 1).[41]

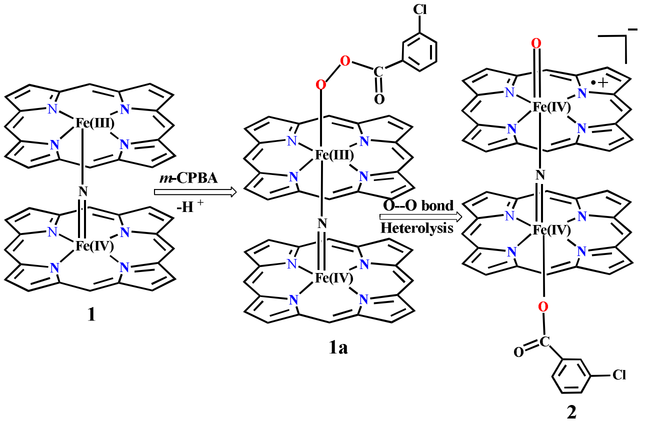

Scheme 1: Formation of *N*-bridged high-valent diiron- oxo complex from Fe(III)-Fe(IV) dimer.

*Electronic structure of [(TPP)Fe(III)(μ-N)Fe(IV)(TPP)] (**1**)*:

Dinuclear species are often difficult to probe due to complex nature of the spin states. The Fe(III) centre in species **1** can be either high-spin (HS) (S=5/2) or intermediate-spin (IS) (S=3/2) or low-spin (LS) (S=1/2) and similarly the Fe(IV) centre can possesses either HS (S=2) or IS (S=1) or LS (S=0) states. These two centres are likely to be coupled via the μ-nitrido bridges leading to ferro/antiferromagnatically coupled states. For species **1**, since the ligand environment is similar for both the metal centres, one can unequivocally assume that both the metal centres are likely to exhibit same type of spin states (.i.e. HS on Fe(III) along with HS on Fe(IV) and IS Fe(III) with IS on Fe(IV) etc). This leads to five possible spin coupled states denoted as $^{10}\mathbf{1}_{(hs,\ hs)}$, $^{2}\mathbf{1}_{(hs,\ hs)}$, $^{6}\mathbf{1}_{(is,\ is)}$, $^{2}\mathbf{1}_{(is,\ is)}$ and $^{2}\mathbf{1}_{(ls,\ ls)}$ as schematically shown in Table 1. Among these spin states, our calculations yield $^{10}\mathbf{1}_{(hs,\ hs)}$, $^{2}\mathbf{1}_{(hs,\ hs)}$ and $^{6}\mathbf{1}_{(is,\ is)}$ spin states correctly while our other two doublets always converge to the $^{2}\mathbf{1}_{(hs,\ hs)}$ state.

Table 1. Different possible spin state configurations in species **1** and **1a**.

	Electronic configuration	
Spin states	**Fe(III)**	**Fe(IV)**
$^{10}\mathbf{1}_{(hs,\ hs)}$	$\delta^{\uparrow}_{xy}\ \pi^{*\uparrow}_{xz}\ \pi^{*\uparrow}_{yz}\ \sigma^{*\uparrow}_{z^2}\ \delta^{\uparrow}_{x^2-y^2}$	$\delta^{\uparrow}_{xy}\ \pi^{*\uparrow}_{xz}\ \pi^{*\uparrow}_{yz}\ \delta^{\uparrow}_{x^2-y^2}\ \sigma^{*}_{z^2}$
$^{2}\mathbf{1}_{(hs,\ hs)}$	$\delta^{\uparrow}_{xy}\ \pi^{*\uparrow}_{xz}\ \pi^{*\uparrow}_{yz}\ \sigma^{*\uparrow}_{z^2}\ \delta^{\uparrow}_{x^2-y^2}$	$\delta^{\downarrow}_{xy}\ \pi^{*\downarrow}_{xz}\ \pi^{*\downarrow}_{yz}\ \delta^{\downarrow}_{x^2-y^2}\ \sigma^{*}_{z^2}$
$^{6}\mathbf{1}_{(is,\ is)}$	$\delta^{\uparrow\downarrow}_{xy}\pi^{*\uparrow}_{xz}\ \pi^{*\uparrow}_{yz}\ \sigma^{*\uparrow}_{z^2}\ \delta_{x^2-y^2}$	$\delta^{\uparrow\downarrow}_{xy}\pi^{*\uparrow}_{xz}\ \pi^{*\uparrow}_{yz}\ \delta_{x^2-y^2}\ \sigma^{*}_{z^2}$
$^{2}\mathbf{1}_{(is,\ is)}$	$\delta^{\uparrow\downarrow}_{xy}\pi^{*\uparrow}_{xz}\ \pi^{*\uparrow}_{yz}\ \sigma^{*\uparrow}_{z^2}\ \delta_{x^2-y^2}$	$\delta^{\uparrow\downarrow}_{xy}\pi^{*\downarrow}_{xz}\ \pi^{*\downarrow}_{yz}\ \delta_{x^2-y^2}\ \sigma^{*}_{z^2}$
$^{2}\mathbf{1}_{(ls,\ ls)}$	$\delta^{\uparrow\downarrow}_{xy}\pi^{*\uparrow\downarrow}_{xz}\pi^{*\uparrow}_{yz}\ \sigma^{*}_{z^2}\ \delta_{x^2-y^2}$	$\delta^{\uparrow\downarrow}_{xy}\pi^{*\uparrow\downarrow}_{xz}\pi^{*}_{yz}\ \delta_{x^2-y^2}\ \sigma^{*}_{z^2}$
$^{10}\mathbf{1a}_{(hs,\ hs)}$	$\delta^{\uparrow}_{xy}\ \pi^{*\uparrow}_{xz}\ \pi^{*\uparrow}_{yz}\ \sigma^{*\uparrow}_{z^2}\ \delta^{\uparrow}_{x^2-y^2}$	$\delta^{\uparrow}_{xy}\ \pi^{*\uparrow}_{xz}\ \pi^{*\uparrow}_{yz}\ \delta^{\uparrow}_{x^2-y^2}\ \sigma^{*}_{z^2}$

Among the three spin states computed, the $^{2}\mathbf{1}_{(hs,\ hs)}$ is found to be the ground state followed by the $^{6}\mathbf{1}_{(is,\ is)}$ state by an energy margin of 25.7 kJ/mol and the $^{10}\mathbf{1}_{(hs,\ hs)}$ state is found lie at 64.7 kJ/mol higher in energy. Our calculations reveal that both the metal centres possess high-spin ground state and this is in line with the experimental observation for similar Fe(III) and Fe(IV) geometries reported earlier.[41] The μ-nitrido bridge mediates a strong delocalization of spin leading to an antiferromagnetic coupling between the two metal centres. Optimized geometries and spin density computed are shown in Figure 1. The Fe(III) centre has the following electronic configuration $(\delta_{xy})^1$ $(\pi^*_{xz})^1$ $(\pi^*_{yz})^1$ $(\sigma^*_{z}{}^{2})^1$ $(\delta_{x}{}^{2}{}_{-y}{}^{2})^1$ while Fe(IV) centre has $(\delta_{xy})^1$ $(\pi^*_{xz})^1$ $(\pi^*_{yz})^1$ $(\delta_{x}{}^{2}{}_{-y}{}^{2})^1$ $(\sigma^*_{z}{}^{2})^0$ electronic configuration for the $^{2}\mathbf{1}_{(hs,\ hs)}$ species (see Figure S1 of ESI). There is a significant π-type interaction between the d_{xz} and d_{yz} orbitals of the two Fe centres via the μ-nitrido bridges and this leads to a very strong antiferromagnetic coupling in this species. The magnetic coupling is estimated using the ground state structure employing the standard protocol[69] and this yields J value of -479.4 cm^{-1} (in $\hat{H} = -J\, S_1{\cdot}S_2$ formalism) and this observation corroborates to the J value expected for the dinuclear iron complexes possessing similar structural motifs.[70-75] The doublet ground state predicted by the calculations is in agreement with the EPR data reported for complex **1**.[41] The Fe-N(1) distances of the $^{2}\mathbf{1}_{(hs,\ hs)}$ state is found to be 1.790 Å and 1.647 Å for the Fe(III) and Fe(IV) site, respectively. As expected the Fe(III)-N(1) distances are longer than the Fe(IV)-N(1) distance for a antiferromagnetic coupled, valance localized states. Although the computed distances are in broad agreement with the X-ray structure reported at 120 K, the Fe(III)-N(1) and Fe(IV)-N(1) distances are predicted to be same in the X-ray structure (1.679 Å). The Wiberg bond index computed for Fe(III)-N(1) and Fe(IV)-N(1) are 1.25 and 1.62 revealing a double bond between Fe and N(1) in case of Fe(IV) centre.

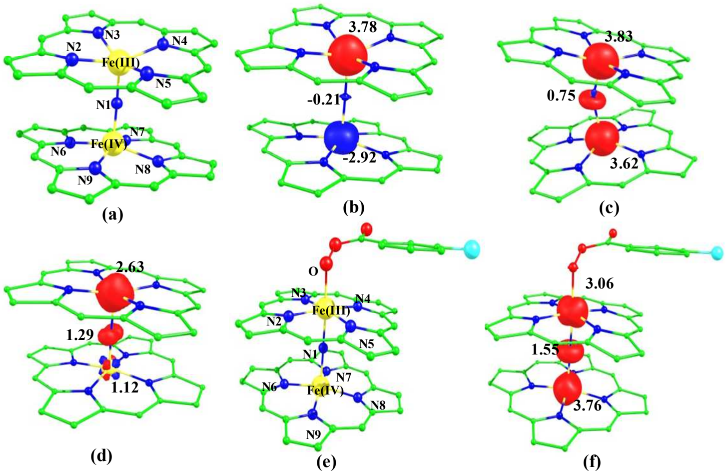

Figure 1: B3LYP-D2 optimized structures of a) $^{2}\mathbf{1}_{(hs,\ hs)}$ state. Spin density plots computed for b) $^{2}\mathbf{1}_{(hs,\ hs)}$ state c) $^{10}\mathbf{1}_{(hs,\ hs)}$ state and d) $^{6}\mathbf{1}_{(is,\ is)}$ state. Optimized structure of e) $^{10}\mathbf{1a}_{(hs,\ hs)}$ state and f) its corresponding spin density plot. The bond parameters computed for the spin states are given below with the following notations $^{2}\mathbf{1}_{(hs,\ hs)}$ ($^{6}\mathbf{1}_{(is,\ is)}$) [$^{10}\mathbf{1}_{(hs,\ hs)}$]. Fe(III)-N1= 1.790 (1.917) [1.828)], Fe(III)-N2= 2.098 (2.075) [2.075], Fe(III)-N3= 2.092 (2.079) [2.080], Fe(III)-N4= 2.094 (2.075) [2.089], Fe(III)-N5= 2.100 (2.082) [2.083], Fe(IV)-N1= 1.647 (1.625) [1.772], Fe(IV)-N6= 2.067 (1.998) [2.076], Fe(IV)-N7= 2.082 (2.012) [2.078], Fe(IV)-N8= 2.070 (1.997) [2.081], Fe(IV)-N9= 2.078 (2.012) [2.082], ∠Fe(III)-N1-Fe(IV)= 158.5 (173.9) [151.7]. For species **1a**, $^{10}\mathbf{1a}_{(hs\ ,hs)}$ Fe(III)-N1= 1.940, Fe(III)-N2= 2.071, Fe(III)-N3= 2.092, Fe(III)-N4= 2.071, Fe(III)-N5= 2.091, Fe(IV)-N1= 1.852, Fe(IV)-N6= 2.069, Fe(IV)-N7= 2.081, Fe(IV)-N8= 2.094, Fe(IV)-N9= 2.088, ∠Fe(IV)-N1-

Fe(IV)= 179.2, ∠N1-Fe(IV)-O= 112.4. All the distances are given in Å and angles in °.

The NBO analysis (see Figure S2 of ESI) further reiterates the nature of Fe-N bonding between the two centres where Fe(III)-N1 bond is found to be strongly σ in character with 30.6% donation from Fe(III) and 69.4% from the N(1) nitrogen atom. The Fe(IV)-N(1) bond on the other hand is found to be covalent in nature with 48.5% contribution from Fe and 51.5% from the N(1) nitrogen atom. For the Fe(IV)-N(1) π-bond, 67.1% and 32.9% donations from Fe and nitrogen atoms respectively have been detected. As expected from the electronic configuration given above, the Fe(IV) centre undergoes Jahn-Teller distortion (axial compression here) possessing longer Fe-N(prop) distances and shorter Fe(IV)-N(1) distance. Since Fe(IV) centre is a Jahn-Teller ion, the structural distortion leads to a valance localization suggesting type I mixed-valance description. Computed spin density plots for all three spin states obtained are shown in Figure 1(b-d). The spin density values on the Fe(III) and Fe(IV) of $^{2}\mathbf{1}_{(hs,\ hs)}$ state are noted as 3.78 and -2.92 suggesting a valance localization of the spins. Significant reduction from the expected value of the spin density suggests that the spin density is delocalized to the coordinated atoms, particularly to the nitrido nitrogen atom (-0.21).

To probe the electronic structure further and to compare and contrast the computed electronic structure with the experimental values, we have computed the spectroscopic parameters of species **1**. The vibrational frequency corresponds to the Fe-N-Fe vibrational mode was computed as 1010 cm^{-1} and this is in agreement with the experimental value of 910 cm^{-1} for the [(TPP)Fe(III)(μ-N)Fe(IV)(TPP)] species. The computed value is also in the range expected for other dinuclear complexes.[36] The computed absorption spectra of $^{2}\mathbf{1}_{(hs,\ hs)}$ state is shown in Figure 2. Calculations reveal three intense peaks at 382, 470 and 520 nm and this agrees well with the experimental observation of three features. The peak observed at 382 nm is found to be metal (π*) to ligand charge transfer band. The peak at 470 nm, pertaining to π* orbital of metal to π* of the ligand orbitals and the peak at 520 nm is assigned as ligand to ligand charge transfer band (see Figure S3 in ESI).

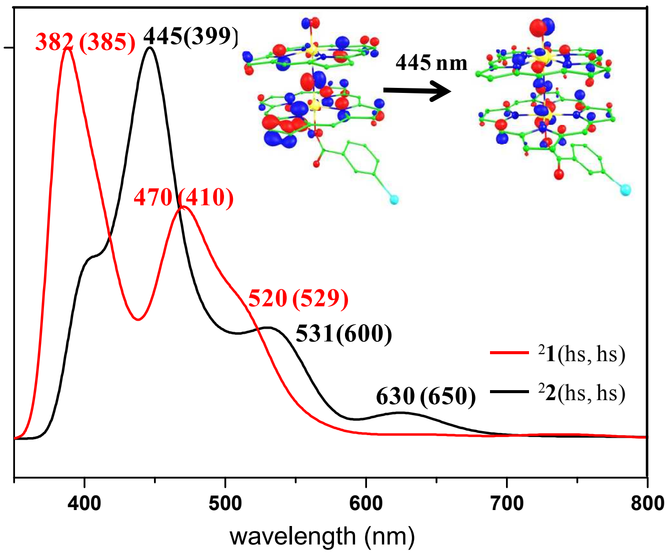

Figure 2. Absorption spectra computed using TD-DFT calculations on the ground state structures of species **1** (red) and **2** (black). The values given in parenthesis are corresponding experimental values.

The g tensor is an integral property of the complexes, and the molecular g tensor can be related to the site tensor values by vector coupling approach where G is the molecular g tensor of the entire system while g_1 and g_2 are the site g-tensor values of the two Fe centres

$$G= c_1g_1+c_2g_2$$

Here c_1 and c_2 are the coefficients for the two cites. Calculations yield G_1= 2.1107 G_2= 2.0117 for $^{2}\mathbf{1}_{(hs,\ hs)}$ state (see Table 2 for individual tensor quantities. Note: to differentiate site g-tensor and molecular g-tensor, G notations are employed throughout) and this is broadly in agreement with the X-band EPR recorded at power sample of **1** (G_1=2.155 and G_2=2.008).[41, 76]

Table 2. Computed spin Hamiltonian parameters for different spin states in species **1**, **1a** and **2**.

Spin states	δ values(mm/s)		ΔE$_Q$ values(mm/s)		g-value		
	Fe(III)	Fe(IV)	Fe(III)	Fe(IV)	G_x	G_y	G_z
$^{10}\mathbf{1}_{(hs,hs)}$	0.50	0.33	0.31	0.16	2.0055	2.0139	2.0164
$^{2}\mathbf{1}_{(hs,hs)}$	0.37	0.13	0.18	1.04	2.0116	2.1039	2.1174
$^{6}\mathbf{1}_{(is,is)}$	0.01	0.51	1.93	-1.44	2.0033	2.0146	2.0361
$^{10}\mathbf{1a}_{(hs,hs)}$	0.54	0.36	-1.51	1.90	2.0128	2.0216	2.0231
$^{10}\mathbf{2}_{(hs,hs)}$	0.44^a	0.18	0.61^a	-1.79	2.0068	2.0163	2.0179
$^{2}\mathbf{2}_{(hs,hs)}$	0.08^a	0.13	-0.13^a	-1.79	2.0132	2.1084	2.2627
$^{8}\mathbf{2}_{(hs,hs)}$	0.08^a	0.13	-1.43^a	-0.49	2.0092	2.0095	2.0183
$^{6}\mathbf{2}_{(is,is)}$	0.25^a	0.05	-2.36^a	0.38	1.9995	2.0364	2.0465

a) for this species the oxidation state of Fe is IV.

Strong deviations from the free electron g-values and significant anisotropy on the estimate of the g-anisotropy reveals that the unpaired electrons are metal based and significant anisotropy computed in the g-tensors are likely due to the Fe(IV) metal centre possessing large spin-orbit coupling. The high-spin Fe(III) centre on the other hand is expected to be isotropic in nature and is unlikely to influence the G-tensor to this extent. The computed isomer shift and quadruple splitting values for $^{2}\mathbf{1}_{(hs,\ hs)}$ state are given in Table 2. The isomer shift computed for the Fe(III) centre is larger than that found for the Fe(IV) centre and this is as expected based on the electron density of core electrons computed. The quadruple shift computed for the two centres are also different, with concomitant larger ΔE_Q for the Fe(IV) centre and smaller one noted for the Fe(III) centre. Among the spin Hamiltonian parameters computed for all three spin states (see Table 2), closer match to experiments[41] was found for the $^{2}\mathbf{1}_{(hs,\ hs)}$ state reiterating the S=1/2 ground state for this species with high-spin configurations on both metal centres coupled in an antiferromagnetic fashion.

Reaction of *m*-CPBA with species **1** is expected to yield [(TPP)Fe(III)(*m*-CPBA)(μ-N)Fe(IV)(TPP)] (**1a**) species (Figure 1).

The spin states expected for this species is similar to that of species **1**. To estimate the energetics of formation of **1a** from species **1**, we have computed the structure and energetics of only the $^{10}\mathbf{1a}_{(hs,\ hs)}$ state. The computed geometry and the spin density plots are shown in Figure 1e and 1f. The energetics of formation of **1a** from **1** is computed to be slightly endothermic in nature (+10.9 kJ/mol) revealing facile coordination of the *m*-CBPA to the Fe(III) site. Upon *m*-CPBA coordination, both the Fe-N(1) distances elongates and the μ-nitrido nitrogen gains significant spin density.

Electronic structure of [(TPP)(*m*-CBA)Fe(IV)(μ-N)Fe(IV)(O)(TPP$^{\bullet+}$)]$^-$ ***(2)***: Heterolytic cleavage of the O-O bond of the *m*-CPBA in species **1a** lead to the formation of [(TPP)(*m*-CBA)Fe(IV)(μ-N)Fe(IV)(O)(TPP$^{\bullet+}$)]$^-$ (**2**) species. As a radical centre is expected to be generated on the TPP ligand, there are seven possible spins states and these are schematically shown in Table 3. Although we have attempted to compute all the seven spin states, convergence was achieved successfully only for the $^{10}\mathbf{2}_{(hs,hs)}$, $^{8}\mathbf{2}_{(hs,hs)}$, $^{2}\mathbf{2}_{(hs,hs)}$, $^{6}\mathbf{2}_{(is,is)}$ and $^{2}\mathbf{2}_{(is,is)}$ states.[77] Here the $^{2}\mathbf{2}_{(hs,hs)}$ state is computed to be the ground state followed by $^{6}\mathbf{2}_{(is,is)}$, $^{2}\mathbf{2}_{(is,is)}$, $^{10}\mathbf{2}_{(hs,hs)}$ and $^{8}\mathbf{2}_{(hs,hs)}$ states at 37.7, 46.2, 402.1 and 266.2 kJ/mol higher in energy, respectively. The computed S=1/2 ground state is consistent with the experiments.[41] The formation energy of species **2** from species **1** is estimated to be -34.6 kJ/mol revealing exothermic nature of the reaction. This suggests that species **1a** is likely to be transient and this reconciles with the lack of strong spectroscopic signature for this species. This energetics computed suggests facile formation of the Fe(IV)=O species upon heterolytic cleavage of the O...O bond in **1a**. The optimized structure of the $^{2}\mathbf{2}_{(hs,hs)}$ state is shown in Figure 3(a).

Table 3. Different possible spin state configurations for species **2**.

	Electronic Configuration		
Spin states	**Fe(IV)**	**Fe(IV)**	**TPP$^{\cdot+}$**
$^{10}\mathbf{2}_{(hs,\ hs)}$	$\delta_{xy}^{\uparrow}\ \pi^*{}_{xz}^{\uparrow}\ \pi^*{}_{yz}^{\uparrow}\ \delta_{x^2-y^2}^{\uparrow}\ \sigma^*{}_{z^2}$	$\delta_{xy}^{\uparrow}\ \pi^*{}_{xz}^{\uparrow}\ \pi^*{}_{yz}^{\uparrow}\ \delta_{x^2-y^2}^{\uparrow}\ \sigma^*{}_{z^2}$	$\uparrow$
$^{8}\mathbf{2}_{(hs,\ hs)}$	$\delta_{xy}^{\uparrow}\ \pi^*{}_{xz}^{\uparrow}\ \pi^*{}_{yz}^{\uparrow}\ \delta_{x^2-y^2}^{\uparrow}\ \sigma^*{}_{z^2}$	$\delta_{xy}^{\uparrow}\ \pi^*{}_{xz}^{\uparrow}\ \pi^*{}_{yz}^{\uparrow}\ \delta_{x^2-y^2}^{\uparrow}\ \sigma^*{}_{z^2}$	$\downarrow$
$^{2}\mathbf{2}_{(hs,\ hs)}$	$\delta_{xy}^{\uparrow}\ \pi^*{}_{xz}^{\uparrow}\ \pi^*{}_{yz}^{\uparrow}\ \delta_{x^2-y^2}^{\uparrow}\ \sigma^*{}_{z^2}$	$\delta_{xy}^{\downarrow}\ \pi^*{}_{xz}^{\downarrow}\ \pi^*{}_{yz}^{\downarrow}\ \delta_{x^2-y^2}^{\downarrow}\ \sigma^*{}_{z^2}$	$\uparrow$
$^{6}\mathbf{2}_{(is,\ is)}$	$\delta_{xy}^{\uparrow\downarrow}\pi^*{}_{xz}^{\uparrow}\ \pi^*{}_{yz}^{\uparrow}\ \delta_{x^2-y^2}\ \sigma^*{}_{z^2}$	$\delta_{xy}^{\uparrow\downarrow}\pi^*{}_{xz}^{\uparrow}\ \pi^*{}_{yz}^{\uparrow}\ \delta_{x^2-y^2}\ \sigma^*{}_{z^2}$	$\uparrow$
$^{4}\mathbf{2}_{(is,\ is)}$	$\delta_{xy}^{\uparrow\downarrow}\pi^*{}_{xz}^{\uparrow}\ \pi^*{}_{yz}^{\uparrow}\ \delta_{x^2-y^2}\ \sigma^*{}_{z^2}$	$\delta_{xy}^{\uparrow\downarrow}\pi^*{}_{xz}^{\uparrow}\ \pi^*{}_{yz}^{\uparrow}\ \delta_{x^2-y^2}\ \sigma^*{}_{z^2}$	$\downarrow$
$^{2}\mathbf{2}_{(is,\ is)}$	$\delta_{xy}^{\uparrow\downarrow}\pi^*{}_{xz}^{\uparrow}\ \pi^*{}_{yz}^{\uparrow}\ \delta_{x^2-y^2}\ \sigma^*{}_{z^2}$	$\delta_{xy}^{\uparrow\downarrow}\pi^*{}_{xz}^{\downarrow}\ \pi^*{}_{yz}^{\downarrow}\ \delta_{x^2-y^2}\ \sigma^*{}_{z^2}$	$\uparrow$
$^{2}\mathbf{2}_{(ls,\ ls)}$	$\delta_{xy}^{\uparrow\downarrow}\pi^*{}_{xz}^{\uparrow\downarrow}\pi^*{}_{yz}\ \delta_{x^2-y^2}\ \sigma^*{}_{z^2}$	$\delta_{xy}^{\uparrow\downarrow}\pi^*{}_{xz}^{\uparrow\downarrow}\pi^*{}_{yz}\ \delta_{x^2-y^2}\ \sigma^*{}_{z^2}$	$\uparrow$

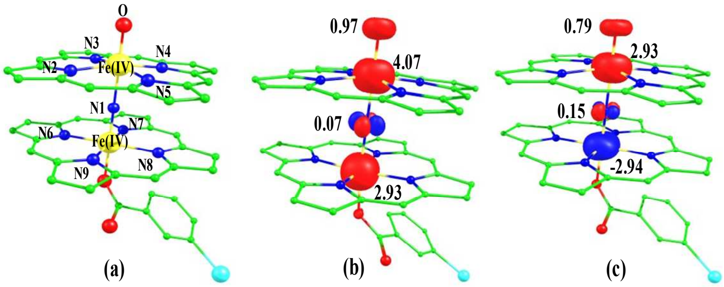

Figure 3: B3LYP-D2 optimized structures of a) $^{2}\mathbf{2}_{(hs,\ hs)}$ state. Spin density plots computed for b) $^{2}\mathbf{2}_{(hs,\ hs)}$ state and c) $^{10}\mathbf{2}_{(hs,\ hs)}$ state. The bond parameters computed for the spin states are given below with the following notations $^{2}\mathbf{2}_{(hs,\ hs)}$ ($^{2}\mathbf{2}_{(is,\ is)}$) {$^{8}\mathbf{2}_{(hs,\ hs)}$} [$^{10}\mathbf{2}_{(hs,\ hs)}$]. Fe(IV)-N1= 1.974 (2.002) {2.008} [2.040], Fe(IV)-N2= 2.078 (2.022) {2.084} [2.086], Fe(IV)-N3= 2.086 (2.022) {2.085} [2.071], Fe(IV)-N4= 2.077 (2.022) {2.085} [2.070], Fe(VI)-N5= 2.087 (2.023) {2.084} [2.098], Fe(IV)-N1= 1.686 (1.876) {1.825} [1.920], Fe(IV)-N6= 2.080 (2.031) {2.010} [2.089], Fe(IV)-N7= 2.093 (2.009) {2.002} [2.088], Fe(IV)-N8= 2.067 (2.020) {2.000} [2.088], Fe(IV)-N9= 2.068 (1.995) {2.008} [2.088], ∠Fe(IV)-N1-Fe(IV)= 177.5 (177.0) {179.4} [179.9], ∠N1-Fe(IV)=O= 179.3 (179.6) {179.8} [178.7]. All the distances are given in Å and angles in °.

For the $^{2}\mathbf{2}_{(hs,hs)}$ state, the Fe(IV)=O bond distance is computed to be 1.661 Å and this estimate is consistent with the experimental values reported for similar Fe(IV)=O species (note the Fe(IV)=O distances reported are in the range of 1.63–1.66 Å for different heme-Fe(IV)=O species[26, 45, 49, 78]). As a consequence of short Fe(IV)=O bond, the bond distance between the bridged nitrogen atom and the Fe(IV) centre have become longer (1.974 Å) while Fe(IV)-N(1) of the second Fe(IV) centre where the *meta*-chlorobenzoate is coordinated has been shortened to 1.686 Å. The Eigen-value plot computed for $^{2}\mathbf{2}_{(hs,hs)}$ state is shown in Figure 4 and here both the Fe(IV) centre has $(\delta_{xy})^1$ $(\pi^*_{xz})^1$ $(\pi^*_{yz})^1$ $(\delta_{x^2-y^2})^1$ $(\sigma^*_{z^2})^0$ electronic configuration leading to Jahn-Teller distortion and longer Fe-N(porp) distances. In both the metal centres, the degeneracy of the π^*_{xz} and π^*_{yz} orbitals is lifted and the radical orbital is found to be significantly destabilized (higher in energy than the $\delta_{x^2-y^2}$ orbital). The computed Wiberg bond index for Fe-N bond in O=Fe(IV)-N(1) and N(1)-Fe(IV)-*m*-CBA are 0.562 and 1.25, indicating single and double bond, respectively. Furthermore, the observed WB index of Fe(IV) and ferryl oxygen (1.35) suggests the presence of a clear double bond between them. Additionally, the computed NBO analysis reveals intrinsic bonding scenario and how the electron distribution presents between the two metal ions. The σ Fe-N bond in O=Fe(IV)-N(1) unit has 26.5 % contribution from the Fe(IV) unit while N(1) contributes 73.5 % (see Figure S5 of ESI). *This unveils a fact that this bond is ionic in nature and has significant donation from the bridging nitrogen atom. On the other hand, the N(1)-Fe(IV) bond in other unit is found to be covalent in nature with 54.5% contribution from Fe(IV) and 45.5 % from N(1). This suggest that the electrons essentially flow from the Fe(IV)-m-CBA unit to the O=Fe(IV) unit and such arrangement likely to enhance the reactivity of the Fe(IV)=O species compared to mononuclear analogues (see Figure S4 of ESI).* The computed spin densities for the complex $^{10}\mathbf{2}_{(hs,hs)}$ and $^{2}\mathbf{2}_{(hs,hs)}$ states are shown in Figure 3 (see ESI Figure S5 for spin density plots for other spin states computed). For the $^{2}\mathbf{2}_{(hs,hs)}$ state, the spin density on the Fe(IV) centres are estimated to be ~2.9 on both Fe centres while significant spin density (0.79) on the ferryl oxygen atom is noted. Although primarily,we have expected a localized radical centre on the TPP ring, calculations reveal that that electrons are completely delocalized to all the atoms including ferryl oxygen atom, μ-nitrido nitrogen atom and the oxygen atom of the *meta*-chlorobenzoate derivatives with spin densities as high as ~0.15 are detected on the nitrogen atoms of the TPP ring.

The computed absorption spectra of $^{2}\mathbf{2}_{(\mathrm{hs,\ hs})}$ state is shown in Figure 2. The TD-DFT calculations yield four intense peaks at 396, 445, 531 and 630 nm. These peak positions corroborate well with the experimental absorption spectra (see Figure 2). The most intense peak observed at 445 nm is found to be N (centred on μ-nitrido nitrogen) to π* (d_{xz}-p_x) transition while the shoulder observed at 531 nm is assigned to π(Fe-O)* to π* TPP ligand transition (see Figure S6 of ESI). The peak observed at 630 nm corresponds to transition from π* TPP ligand to π(Fe-N-Fe-O)* orbital. Magnetic coupling between the two Fe(IV) centres are estimated to be antiferromagnetic in nature with the estimate of J being -225 cm^{-1} (in $\hat{H}= -J\, S_1 \cdot S_2$ formalism).

Experiments suggest very strong antiferromagnetic interaction between the two metal centres and the computed J support this argument.[41] The computed g-tensors for species **2** are given in Table 2. Calculations yield a rhombic set of G-values (G_x=2.0132, G_y=2.1084 and G_z=2.2627) for $^{2}\mathbf{2}_{(\mathrm{hs,\ hs})}$ state while for all other spin states, the computed G-values are nearly isotropic in nature.

The frozen solution X-band EPR spectra recorded at 120 K for this species however yield an isotropic g-values (estimated G=2.001).[41, 76]

This suggests that apart from the ground state, other spin states might also have contributed to the observed experimental G-values. The computed isomer shift and quadruple splitting values for $^{2}\mathbf{2}_{(\mathrm{hs,\ hs})}$ state are given in Table 2.

Calculations yield two distinct isomer shift values with a very small value for the Fe(IV)=O centre and slightly larger value for the Fe(IV)-*m*-CBA centre. Similarly the ΔE_Q values are noted to be distinctly different for both the sites with smaller ΔE_Q value for the Fe(IV)=O centre and larger value for the Fe(IV)-*m*-CBA site. Experimental Mössbauer spectra recorded at 4.2 K for species **2** yields two satisfactory fits and these values are given in Table 2. The second set of the fit parameters are found to comply with the calculated data betterthan the first set.[41] Although dissymmetry (different isomer shift and ΔE_Q for the two Fe centres) are observed in the experiments, due to low signal-to-noise ratio of the recorded spectra, the individual values have not been extracted.

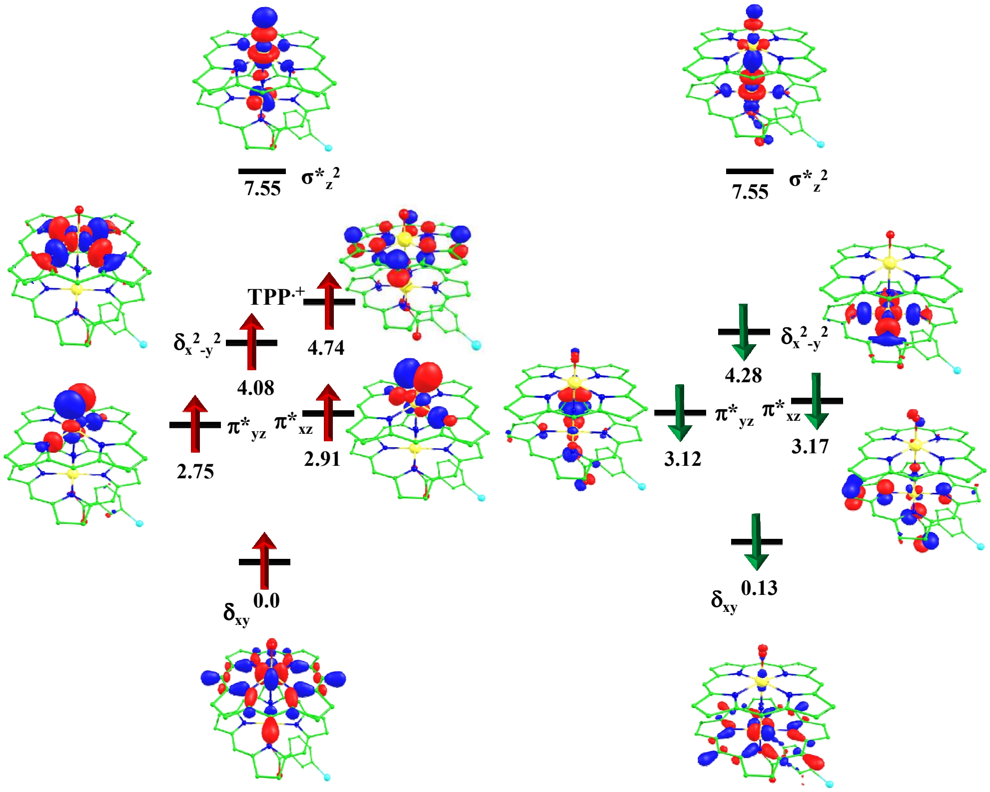

Figure 4. B3LYP-D2 computed Eigen-value plot incorporating energies computed for d-based orbitals for alpha and beta spin of $^{2}\mathbf{2}_{(\mathrm{hs,\ hs})}$ species (energies are given in eV).

Mechanism of C-H activation of methane by 2:

The Fe(IV)=O unit present in species **2** is proposed as an active oxidant responsible for alkane hydroxylationto variety of substrates such as cyclohexane, adamentane, ethylbenzene and methane.[41, 49, 79] Methane oxidation under turnover conditions by **2** yield, turnover number as high as 13.7 revealing strong oxidizing ability of the species **2**. Here we have attempted to explore the intrinsic mechanism of methane activation by this species as this is an extremely important reaction from both industrial and green chemistry perspectives. Schematic mechanism proposed based on the experimental evidence and earlier precedence on the cytochrome P450 and MMO reactivity is shown in Scheme 2.[4, 6, 44, 80, 81]

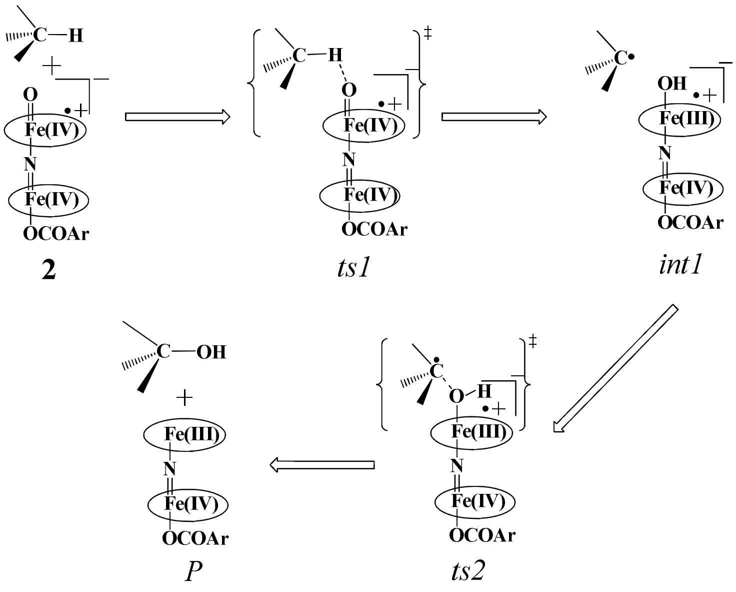

Scheme 2: Schematic mechanism proposed for C-H bond activation of methane by species **2**.

In the first step, the C-H activation of the methane by the Fe(IV)=O unit is assumed via *ts1*. This is preceded by the formation of Fe(III)-OH intermediate (*int1*). In the next step rebounding of the -OH group is assumed to take place via (*ts2*) leading to the formation of methanol. The rebound mechanism for the hydroxylation of alkanes and alkenes is thoroughly explored and significant experimental evidence for this mechanism has been accumulated.[80-82] The five spin states computed for species **2** have been employed to construct the potential energy surface (PES) for the methane oxidation as described in the above scheme (see Figure 5). Among five possible transition states, $^{10}ts1_{(hs,hs)}$, $^{2}ts1_{(hs,hs)}$ and $^{2}ts1_{(is,is)}$ transition states were successfully optimized. The $^{2}ts1_{(hs,hs)}$ is characterized by a single imaginary frequency (-1292 cm^{-1}) and has a barrier height of 56.6 kJ/mol. However this is not the lowest energy pathway as $^{2}ts1_{(is,is)}$ transition state is found to have the barrier height of just 26.6 kJ/mol from the $^{2}\mathbf{2}_{(hs,hs)}$ surface. This certainly demands a mean-energy crossing point (MECP)[83] between the two spin surface and given the large anisotropy and spin-orbit coupling estimated for these states, we expect that, this spin-crossover is likely to be facile. The orbital evolution diagram for the C-H bond activation for $^{2}ts1_{(is,is)}$ and $^{2}ts1_{(hs,hs)}$ are shown in Figure 6. No significant exchange enhanced reactivity is expected for the high-spin state at π-type pathway.[84] Besides, as significant spin density has been found at the μ-nitrido atom and it is strongly bound to the metal centre via the σ and π interaction, the electron delocalization to $\sigma^{*}z^{2}$ is presumably expected for this species. For these reasons, the C-H bond activation even at high-spin state is found to occur via the π-channel. For the $^{2}ts1_{(is,is)}$ state as well, no gain in exchange enhanced reactivity is seen and significant reduction in the barrier height is primarily due to the orbital controlled nature of the reaction. Additionally weak C-H..π interactions between methane and the TPP ring is expected to fix the methane on the TPP surface and thus activate π-type reactivity. The estimated barrier height of 26.6 kJ/mol for C-H bond activation of methane is remarkably low for species **2**. For the cytochrome P450, earlier theoretical studies have estimated the barrier heights to be 110.8 kJ/mol while theoretical calculations performed on model systems of dinuclear MMO estimates the barrier height to be 81.6 kJ/mol (Note there are some minor deviations in the theoretical methodology employed here and the literature values quoted). Despite these higher barriers computed for these two enzymes, they are naturally superior to species **2** as enzymatic conditions are very different compared to the bio-mimic systems. This also highlights the fact that for the model systems, the kinetic barrier heights lower than that of enzymes are desired to demonstrate the oxidizing abilities at laboratory conditions.

The next question obviously arises is, what is the reason for lower barrier heights for the C-H bond activation compared to P450 models? Due to the dinuclear nature of the model system, the Fe(IV)=O species possesses stronger electron delocalization than the corresponding mononuclear analogues. Here the {Fe(IV)(O)(TPP$^{\bullet+}$)} unit has {(TPP)(*m*-CBA)Fe(IV)(N)} unit as the axial ligand and the μ-nitrido groups possessing significant spin density and its accrual of electron from the {(TPP)(*m*-CBA)Fe(IV)} unit clearly reveals the cooperativity between two iron centres on the reactivity. The spin density plot (Figure 3c) clearly reveals a spin polarization at the Fe(IV)=O centre (gain of spin density on the Fe(IV)=O unit at the transition state) and the existence of cooperative oxidizing ability of the combined unit. The second unit present also helps to stabilize the newly forming Fe(III)O-H bond thus enhancing the reactivity further. Earlier experimental and theoretical studies on axial ligand effect on [Fe(IV)(O)(porp$^{\bullet+}$)(X)] species clearly demonstrate that electron donating group significantly increase the reactivity and this supports our observation.[26]

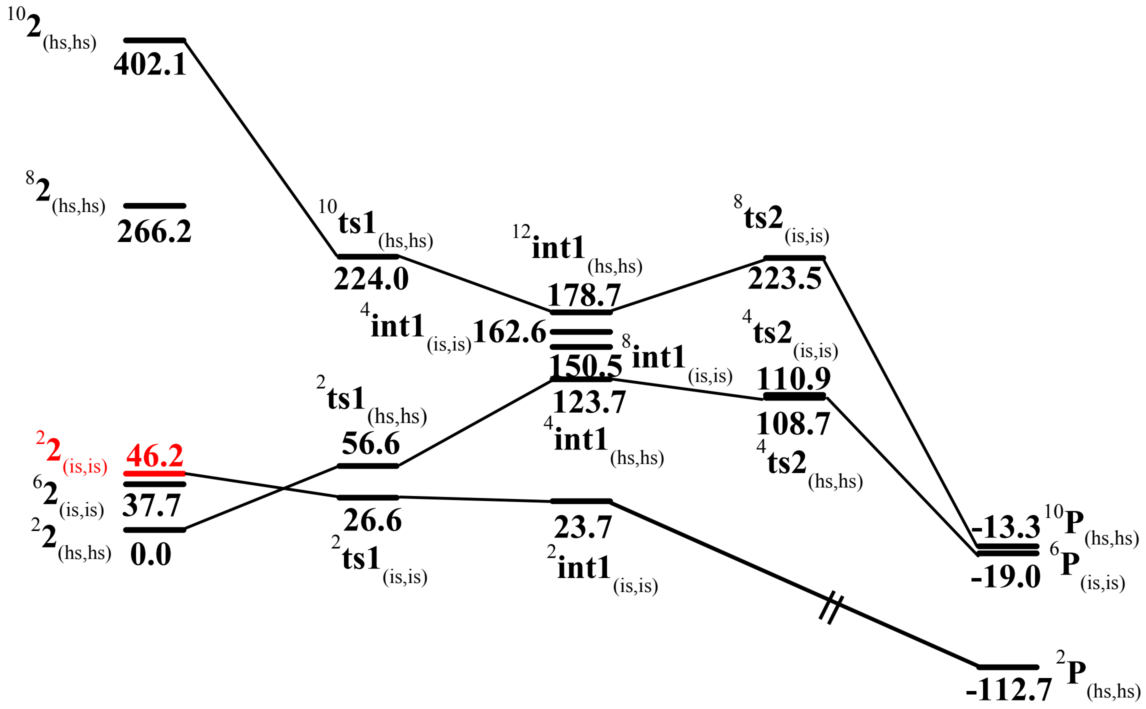

Figure 5: B3LYP-D2computed potential energy surface for C-H bond activation of methane by species **2**. (kJ/mol).

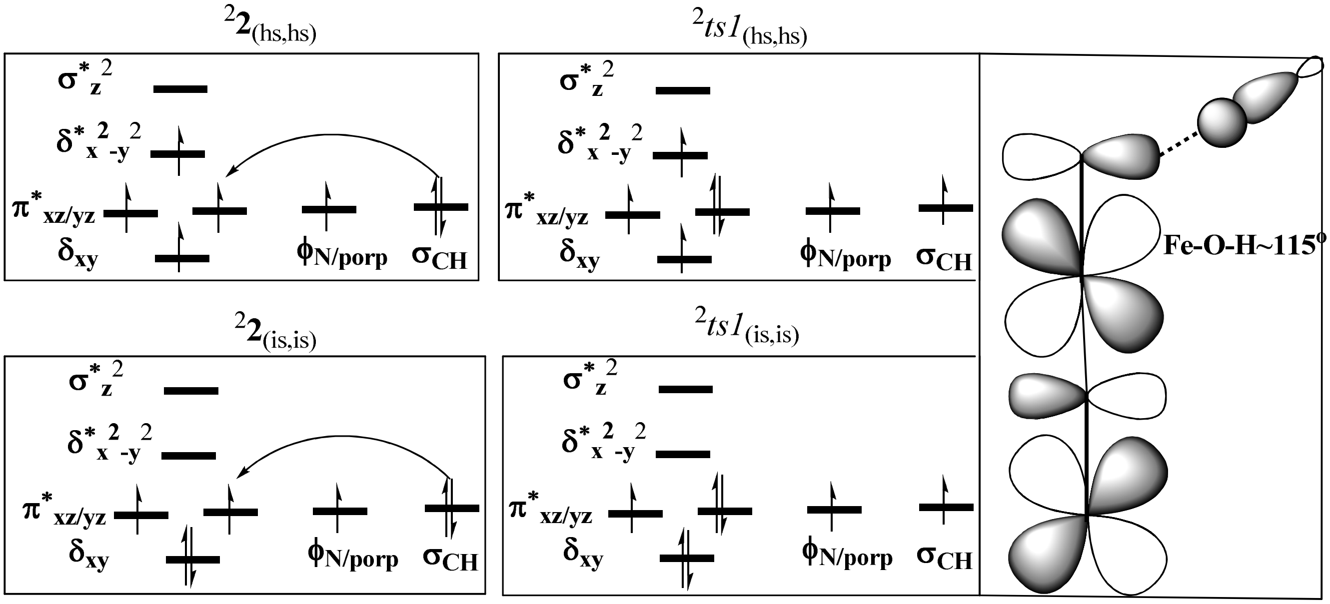

Figure 6: The orbital evolution diagram for the C-H activation for ^{2}*ts1*$_{(is,is)}$ and^{2}*ts1*$_{(hs,hs)}$

The ∠Fe-O...H angle is estimated to be 113.8 degree revealing rather π-type pathway for the hydrogen atom abstraction reaction.[84, 85] The optimized structure and the corresponding spin density plot of the $^{2}ts1_{(is,is)}$ is shown in Figure 6 (see also Table S1 of ESI). The Fe-O bond in $^{2}ts1_{(is,is)}$ elongates to 1.844 Å compared to its bond length in the Fe(IV)=O reactant (1.673 Å) and at the same time the Fe-N(1) bond length shortens. The newly forming O1…H1 bond in the transition states is computed to be 1.123 Å (see Figure 6) suggesting that O-H bond is fully formed at the transition state while the H1---C1 bond is nearly broken (1.418 Å). The computed energy profile diagram is depicted in Figure 4. At the transition state as the H1---C1 bond is broken; this subsequently spurs the generation of radical character at the carbon atom suggesting HAT type reaction.[48, 86]

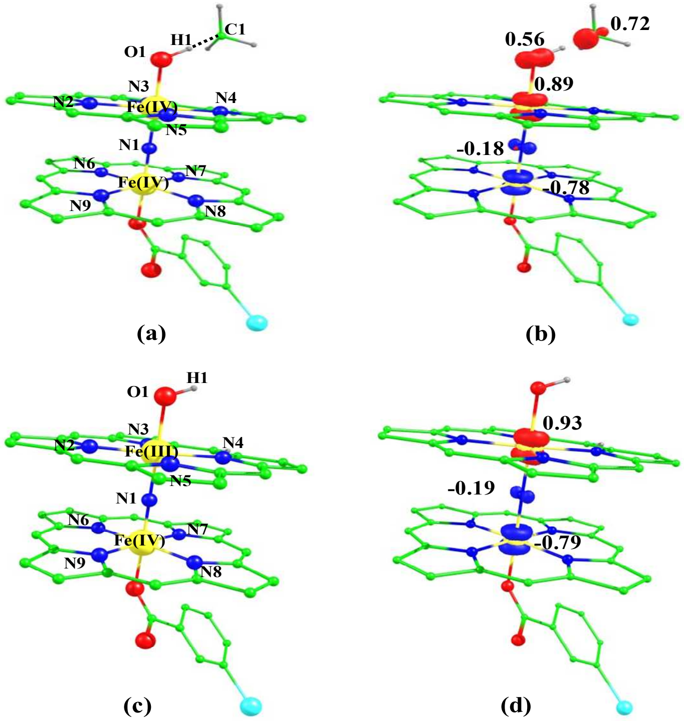

Figure 6: B3LYP-D2 optimized structure of a) $^{2}ts1_{(is,\ is)}$ state. Spin density plot computed for b) $^{2}\mathbf{2}_{(hs,\ hs)}$ state. Optimized structure of c) $^{2}int1_{(is,\ is)}$ state and d) its corresponding spin density plot. The bond parameters computed for the spin states are given below with the following notations $^{2}ts1_{(is,\ is)}$ ($^{2}ts1_{(hs,\ hs)}$) [$^{10}ts1_{(hs,\ hs)}$] Fe(IV)-N1= 1.718 (1.749) [1.761], Fe(IV)-N2= 2.018 (2.070) [2.083], Fe(IV)-N3= 2.020 (2.087) [2.085], Fe(IV)-N4= 2.018 (2.068) [2.078], Fe(VI)-N5= 2.023 (2.090) [2.085], Fe(IV)-N1= 1.649 (1.677) [2.030], Fe(IV)-N6= 2.018 (2.065) [2.088], Fe(IV)-N7= 2.023 (2.098) [2.092], Fe(IV)-N8= 2.018 (2.064) [2.065], Fe(IV)-N9= 2.011(2.077) [2.074], Fe(IV)-O1= 1.844 (1.827) [1.857], O1-H1= 1.123 (1.129) [1.125], H1-C1= 1.418 (1.410) [1.420], ∠Fe(IV)-N1-Fe(IV)= 179.4 (179.0) [179.1], ∠N1-Fe(IV)-O= 177.7 (178.1) [177.8], ∠Fe(IV)-O1-H1= 113.9 (113.9) [115.2], ∠O1-H1-C1= 179.1 (178.4) [176.3]. For species *int1,* $^{2}int1_{(is,\ is)}$ ($^{4}int1_{(hs,hs)}$) {$^{8}int1_{(is,\ is)}$} [$^{4}int1_{(is,\ is)}$] $^{12}int1_{(hs,hs)}$. Fe(III)-N1= 1.697 (2.061) {2.193} [1.838] 2.180, Fe(III)-N2= 2.023 (2.102) {2.069} [2.021] 2.112, Fe(III)-N3= 2.021 (2.113) {2.022} [2.026] 2.098, Fe(III)-N4= 2.015 (2.100) {2.036} [2.017] 2.072, Fe(III)-N5= 2.025 (2.078){2.020} [2.018] 2.098, Fe(IV)-N1= 1.651 (1.795) {1.865} [1.717] 1.884, Fe(IV)-N6= 2.017 (2.007) {2.032} [2.027] 2.070, Fe(IV)-N7= 2.024 (2.008) {2.011} [2.020] 2.095, Fe(IV)-N8= 2.017 (2.001) {2.021} [2.016] 2.070, Fe(IV)-N9= 2.012 (2.001) {1.998} [2.005] 2.074, O1-H1= 0.981 (0.977) {0.979} [0.982] 0.976, ∠Fe(III)-N1-Fe(IV)= 179.6 (177.7) {179.0} [179.3] 178.6, ∠N1-Fe(III)-O= 179.1 (175.7) {175.8} [178.5] 173.8, ∠Fe(III)-O1-H1= 108.7 (119.3) {117.5} [108.3] 123.4. All the distances are given in Å and angles in °.

In the next step, the Fe(III)-OH formation get accomplished leading to the formation of *int1*. For the intermediate, we have computed $^{2}int1_{(is,is)}$, $^{4}int1_{(hs,hs)}$, $^{8}int1_{(is,is)}$, $^{4}int1_{(is,is)}$ and $^{12}int1_{(hs,hs)}$ states (Note that the spin state of the methyl radical is assumed to be at spin-up state and thus the spin multiplicity of all the species are raised by one more unpaired electron). Here the $^{2}int1_{(is,is)}$ is found to be low lying with just 3 kJ/mol lower than the transition state $^{2}ts1_{(is,is)}$, revealing endothermic nature of the reaction. Other intermediates are computed to be much higher in energy with $^{4}int1_{(hs,hs)}$ state lying 100 kJ/mol higher compared to $^{2}int1_{(is,is)}$ state (See Figure 4 for other state energies). Also for cytochrome P450, this step is computed to be endothermic in nature, revealing resemblance in the energetic landscape despite significant structural/electronic differences.[80, 82, 87] In $^{2}int1_{(is,is)}$ intermediate, the Fe-O and the O-H bonds are computed to be 1.865 Å and 0.981 Å revealing complete bond formation and also indicating single bond nature of Fe-OH bond. The Fe(III)-N(1) distance is computed to be 1.697 Å implying shortening of the Fe-N distance compared to transitions state and the reactant. The N(1)-Fe(IV) bond on the other hand remains almost similar throughout (here it is 1.651 Å). Shortening of the Fe(III)-N(1) distance delineates strong electron delocalization and in fact the spin density distribution further indicates a complete delocalization of spin with +3.5 oxidation state on both the metal centres. This additional flexibility available enhances the reactivity. In the next step rebound of the O-H group to the methyl radical is expected to take place. Here we have calculated $^{4}ts2_{(is,\ is)}$, $^{8}ts2_{(is,\ is)}$ and $^{4}ts2_{(hs,\ hs)}$ transitions states and $^{4}ts2_{(hs,\ hs)}$ is found to be the lowest in energy and its barrier height is found to be 85.0 kJ/mol followed by 87.2 and 199.8 kJ/mol for $^{4}ts2_{(is,\ is)}$ and $^{8}ts2_{(is,\ is)}$ respectively (from $^{2}int1_{(is,is)}$ state). Our attempt to obtain $^{2}ts2_{(is,\ is)}$ transition state corresponding to the lowest lying intermediate was not successful and generally on doublet surface the rebound step is barrier-less as it has been demonstrated earlier for both heme and non-heme Fe(IV)=O hydroxylation reactions.[87] We believe that a similar barrier-less process is operational also for the second step leading to the formation of methanol. The optimized structure and spin density plot of the ground state of $^{4}ts2_{(hs,\ hs)}$ are shown in Figure 7. For the $^{4}ts2_{(hs,\ hs)}$ transitions state, the Fe-O bond is further elongated (1.901 Å) compared to the intermediate and the newly forming O1-C1 bond is computed to be 2.488 Å revealing a reactant like transition state with no significant bonding interaction between the ferryl oxygen and the carbon atom of the methyl radical. This also adds significance to our earlier statement on barrier-less reaction on doublet surface as here spin-up position on the radical centre lead to significant electron repulsion and thus very long O1...C1 bond distances at the transition state. Significant increase of spin density at the carbon atom (1.0) in transition state reveals that the spin polarization is operational. The computed barrier height at this surface is very high compared to P450 models where the barrier height is computed to be 23 kJ/mol. Clearly one of the reason for very large barrier height at this surface is the significant electron repulsion as delocalization of methyl radical spin is not seen and also the Fe(III)-OH bond being stronger adds up significant energy penalty (see Figure 7). [88]

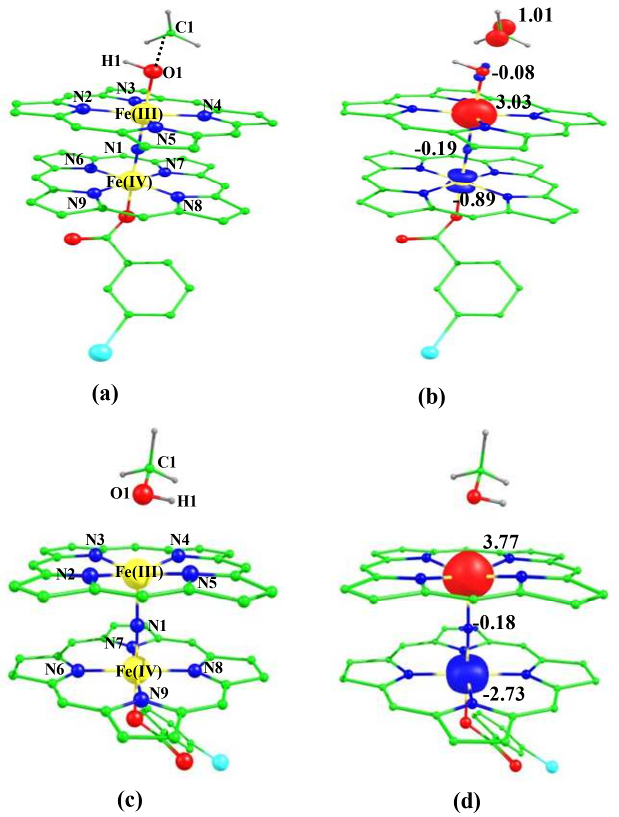

Figure 7: B3LYP-D2 optimized structure of a) $^{4}ts2_{(hs,\ hs)}$ state. Spin density plot computed for b) $^{4}ts2_{(hs,\ hs}$ state. Optimized structure of c) $^{2}P_{(hs,hs)}$ state and d) its corresponding spin density plot. The bond parameters computed for the spin states are given below with the following notations $^{4}ts2_{(hs,\ hs)}$ ($^{4}ts2_{(is,\ is)}$) [$^{8}ts2_{(is,\ is)}$]. Fe(III)-N1= 1.719 (1.886) [1.952], Fe(III)-N2= 2.073 (2.061) [2.064], Fe(III)-N3= 2.075 (2.105) [2.098], Fe(III)-N4= 2.083 (2.052) [2.061], Fe(III)-N5= 2.097 (2.110) [2.099], Fe(IV)-N1= 1.649 (1.742) [1.880], Fe(IV)-N6= 2.028 (2.021) [2.029], Fe(IV)-N7= 2.016 (2.024) [2.009], Fe(IV)-N8= 2.011 (2.012) [2.019], Fe(IV)-N9= 2.015 (2.010) [1.996], Fe(III)-O1= 1.901 (1.861) [1.856], O1-H1= 0.982 (0.983) [0.983], O1-C1= 2.488 (2.415) [2.441], ∠Fe(III)-N1-Fe(IV)= 179.5 (178.2) [174.9], ∠Fe(III)-O1-H1= 108.0 (111.4) [111.6], ∠Fe(III)-O1-C1= 128.3 (135.8) [135.4]. For species *P*, $^{2}P_{(hs,hs)}$ ($^{6}P_{(is,is)}$) [$^{10}P_{(hs,hs)}$]. Fe(III)-N1= 1.773 (1.743) [1.951], Fe(III)-N2= 2.108 (2.027) [2.090], Fe(III)-N3= 2.121 (2.029) [2.102] , Fe(III)-N4= 2.085 (2.010) [2.069], Fe(III)-N5= 2.082 (2.013) [2.079], Fe(IV)-N1= 1.652 (2.089) [1.855], Fe(IV)-N6= 2.078 (2.026) [2.088], Fe(IV)-N7= 2.095 (2.032) [2.088], Fe(IV)-N8= 2.075 (2.015) [2.086], Fe(IV)-N9= 2.073 (2.022) [2.069], Fe(IV)-O1= 2.468 (2.183) [2.285], O1-H1= 0.981 (0.983) [0.979], O1-C1= 1.457 (0.979) [1.462], ∠Fe(III)-N1-Fe(IV)= 178.6 (179.7) [179.4], ∠Fe(III)-O1-H1= 85.6 (98.1) [96.9], ∠Fe(III)-O1-C1= 116.4 (116.7) [116.3]. All the distances are given in Å and angles in °.

Conclusions:

Activation of inert C-H bonds such as that of methane has been a great challenge in the area of catalysis. Despite the fact that several enzymes perform oxidation of methane readily, a biomimic complex which could do this transformation efficiently was rare. Report of N-bridged high-valent diiron(IV)-oxo possessing additional cationic-radical character found to oxidize methane readily, is a significant breakthrough in this area. Here using density functional methods we have explored the electronic structure and mechanism of methane activation by this species. Conclusions derived from our work is summarized below,

(i) The dinuclear reactant species [(TPP)Fe(III)(μ-N)Fe(IV)(TPP)](**1**) is found to possess doublet valance localized ground state. Absorption spectra indicates low-energy ligand to ligand transition indicating possibility of ligand oxidation at lower potential, while computed g-anisotropy yields anisotropic G-tensors revealing significant spin-orbit coupling at the Fe(IV) centre.

(ii) Reaction of **1** with *m*-CPBA is found to be facile and yields an *m*-CPBA coordinated species by an endothermic reaction and this species quickly undergoes heterolytic cleavage of the O-O bond of the *m*-CPBA leading to the formation of the catalytically active [(TPP)(*m*-CBA)Fe(IV)(μ-N)Fe(IV)(O)(TPP$^{\bullet+}$)]$^{-}$(**2**) by an exothermic reaction. Calculations reveal that the two iron centres in species **2** are strongly antiferromagnetically coupled while the radical centres are found to significantly delocalize to many atoms including μ-nitrido nitrogen atom nitrogen atoms of the porphyrin ring etc. Intricate bonding analysis reveal that the Fe(IV)=O centre accepts electron from the μ-nitrido nitrogen atom which in turn accepts donation from the Fe(IV)-*m*-CBA unit. The computed spectroscopic parameters are broadly in agreement with the experiments.

(iii) Extremely small activation energy for C-H bond activation of methane was detected for species **2** and the reaction was in fact found to proceed via a the exited intermediate-spin state of Fe(IV) centre rather than the high-spin ground state. Preferential π-type reactivity is observed at all spin states and orbital control nature of the reaction was found to lead to a significant reduction in barrier height at the intermediate-spin state of Fe(IV)=O species. The formation of the radical intermediate is found to be endothermic in nature at all spin states while the rebound step is expected to be barrier-less at the doublet surface. The computed rebound step at other spin surfaces yield very high barrier for the -OH rebound reaction.

(iv) Overall an electronic cooperativity between two metal centres throughout the catalytic reactions is witnessed and this leads to an extremely lower barrier height, stronger Fe(III)-OH bond at the intermediate and lower barriers for the rebound step. All these lead to very high turnover numbers for methane oxidation per catalytically active species. Comparison of our calculated results to earlier report on cytochrome P450 and MMO models reveal that biomimic models should possess significantly lower barrier height than the enzymes to demonstrate catalytic abilities at the laboratory conditions.

To this end, here for the first time using DFT methods we have described a subtle electronic structure of a μ-nitrido bridged dinuclear iron(IV)-oxo species and unravel the oxidation of methane by this species. The idea of electronic cooperativity presented here has wider scope on the other dinuclear models/enzymes.

Acknowledgements

GR would like to thank the INSA, AISRF and DST Nanomission (SR/NM/NS-1119/2011) for funding. NV would like to thank the DST for fast track fellowship (CS-338/2011).MA and AA thanks CSIR/IIT Bombay for a fellowship.

Notes and References:

†Prof. Gopalan Rajaraman, Associate Professor, Department of Chemistry, Indian Institute of Technology Bombay, Powai, Mumbai-400076. Email: rajaraman@chem.iitb.ac.in

Electronic Supplementary Information (ESI) available: Eigen values plots, NBO plots, Table for energy, optimized parameters, spin density,.See DOI: 10.1039/b000000x/

1. D. A. Whittington, M. H. Sazinsky and S. J. Lippard, *J. Am. Chem. Soc.*, 2001, **123**, 1794-1795.
2. V. Guallar, B. F. Gherman, W. H. Miller, S. J. Lippard and R. A. Friesner, *J. Am. Chem. Soc.*, 2002, **124**, 3377-3384.
3. C. E. Tinberg and S. J. Lippard, *Acc. Chem. Res.*, 2011, **44**, 280-288.
4. G.-D. Roiban, R. Agudo and M. T. Reetz, *Angew. Chem. Int. Ed.*, 2014, **53**, 8659-8663.
5. A. F. W. Coulson and T. Yonetani, *Biochemistry*, 1975, **14**, 2389-2396.
6. D. Hamdane, H. Zhang and P. Hollenberg, *Photosynth. Res.*, 2008, **98**, 657-666.
7. B. J. Wallar and J. D. Lipscomb, *Chem. Rev.*, 1996, **96**, 2625-2658.
8. X. Shan and L. Que Jr, *J. Inorg. Biochem.*, 2006, **100**, 421-433.
9. E. Y. Tshuva and S. J. Lippard, *Chem. Rev.*, 2004, **104**, 987-1012.
10. C. Kim, Y. Dong and L. Que, *J. Am. Chem. Soc.*, 1997, **119**, 3635-3636.
11. B. Modén, B.-Z. Zhan, J. Dakka, J. G. Santiesteban and E. Iglesia, *J. Phys. Chem. C*, 2006, **111**, 1402-1411.
12. X. Li, R. Fu, S. Lee, C. Krebs, V. L. Davidson and A. Liu, *Porc. Nat. Acad. Sci., USA*, 2008, **105**, 8597-8600.
13. J. T. Groves, *J. Inorg. Biochem.*, 2006, **100**, 434-447.
14. S. Hong, H. So, H. Yoon, K.-B. Cho, Y.-M. Lee, S. Fukuzumi and W. Nam, *Dalton Trans.*, 2013, **42**, 7842-7845.
15. D. Lee, J. D. Bois, D. Petasis, M. P. Hendrich, C. Krebs, B. H. Huynh and S. J. Lippard, *J. Am. Chem. Soc.*, 1999, **121**, 9893-9894.
16. P. Comba, H. Wadepohl and S. Wunderlich, *Eur. J. Inorg. Chem.*, 2011, **2011**, 5242-5249.
17. P. Comba, H. Wadepohl and S. Wiesner, *Eur. J. Inorg. Chem.*, 2011, **2011**, 2610-2615.
18. P. Comba, H. Wadepohl and A. Waleska, *Aust. J. Chem.*, 2014, **67**, 398-404.
19. P. Comba, M. Morgen and H. Wadepohl, *Inorg. Chem.*, 2013, **52**, 6481-6501.
20. P. Comba, Y.-M. Lee, W. Nam and A. Waleska, *Chem. Commun.*, 2014, **50**, 412-414.
21. M. Jaccob, P. Comba, M. Maurer, P. Vadivelu and P. Venuvanalingam, *Dalton Trans.*, 2011, **40**, 11276-11281.
22. S. Fukuzumi, Y. Morimoto, H. Kotani, P. Naumov, Y.-M. Lee and W. Nam, *Nat. Chem.*, 2010, **2**, 756-759.
23. A. J. McGown, W. D. Kerber, H. Fujii and D. P. Goldberg, *J. Am. Chem. Soc.*, 2009, **131**, 8040-8048.
24. A. R. McDonald and L. Que Jr, *Coord. Chem. Rev.*, 2013, **257**, 414-428.
25. M. H. Lim, J.-U. Rohde, A. Stubna, M. R. Bukowski, M. Costas, R. Y. N. Ho, E. Münck, W. Nam and L. Que, *Proc. Nat. Acad. Sci. USA.*, 2003, **100**, 3665-3670.
26. Y. Kang, H. Chen, Y. J. Jeong, W. Lai, E. H. Bae, S. Shaik and W. Nam, *Chem. Eur. J.*, 2009, **15**, 10039-10046.
27. A. Takahashi, D. Yamaki, K. Ikemura, T. Kurahashi, T. Ogura, M. Hada and H. Fujii, *Inorg. Chem.*, 2012, **51**, 7296-7305.
28. A. B. Sorokin, S. Mangematin and C. Pergrale, *J. Mol. Catal. A: Chem.*, 2002, **182–183**, 267-281.
29. L. A. Bottomley, J. N. Gorce, V. L. Goedken and C. Ercolani, *Inorg. Chem.*, 1985, **24**, 3733-3737.
30. C. Ercolani, M. Gardini, G. Pennesi, G. Rossi and U. Russo, *Inorg. Chem.*, 1988, **27**, 422-424.
31. G. Rossi, M. Gardini, G. Pennesi, C. Ercolani and V. L. Goedken, *J. Chem. Soc., Dalton Trans.*, 1989, 193-195.
32. C. Ercolani, S. Hewage, R. Heucher and G. Rossi, *Inorg. Chem.*, 1993, **32**, 2975-2977.
33. C. Ercolani, J. Jubb, G. Pennesi, U. Russo and G. Trigiante, *Inorg. Chem.*, 1995, **34**, 2535-2541.
34. M. P. Donzello, C. Ercolani, K. M. Kadish, Z. Ou and U. Russo, *Inorg. Chem.*, 1998, **37**, 3682-3688.
35. M. P. Donzello, C. Ercolani, U. Russo, A. Chiesi-Villa and C. Rizzoli, *Inorg. Chem.*, 2001, **40**, 2963-2967.
36. A. B. Sorokin, *Chem. Rev.*, 2013, **113**, 8152-8191.
37. A. B. Sorokin, E. V. Kudrik and D. Bouchu, *Chem. Commun.*, 2008, 2562-2564.
38. A. B. Sorokin, E. V. Kudrik, L. X. Alvarez, P. Afanasiev, J. M. M. Millet and D. Bouchu, *Catal. Today*, 2010, **157**, 149-154.
39. E. V. Kudrik and A. B. Sorokin, *Chem. Eur. J.*, 2008, **14**, 7123-7126.
40. U. Isci, P. Afanasiev, J.-M. M. Millet, E. V. Kudrik, V. Ahsen and A. B. Sorokin, *Dalton Trans.*, 2009, 7410-7420.
41. E. V. Kudrik, P. Afanasiev, L. X. Alvarez, P. Dubourdeaux, M. Clémancey, J.-M. Latour, G. Blondin, D. Bouchu, F. Albrieux, S. E. Nefedov and A. B. Sorokin, *Nat. Chem.*, 2012, **4**, 1024-1029.
42. P. Afanasiev, E. V. Kudrik, J.-M. M. Millet, D. Bouchu and A. B. Sorokin, *Dalton Trans.*, 2011, **40**, 701-710.
43. C. Colomban, E. V. Kudrik, V. Briois, J. C. Shwarbrick, A. B. Sorokin and P. Afanasiev, *Inorg. Chem.*, 2014, **53**, 11517-11530.
44. H. Basch, K. Mogi, D. G. Musaev and K. Morokuma, *J. Am. Chem. Soc.*, 1999, **121**, 7249-7256.
45. P. E. M. Siegbahn and R. H. Crabtree, *J. Am. Chem. Soc.*, 1997, **119**, 3103-3113.
46. M.-H. Baik, M. Newcomb, R. A. Friesner and S. J. Lippard, *Chem. Rev.*, 2003, **103**, 2385-2420.

47. R. Silaghi-Dumitrescu, S. V. Makarov, M.-M. Uta, I. A. Dereven'kov and P. A. Stuzhin, *New J. Chem.*, 2011, **35**, 1140-1145.
48. M. Jaccob, A. Ansari, B. Pandey and G. Rajaraman, *Dalton Trans.*, 2013, **42**, 16518-16526.
49. A. Ansari, A. Kaushik and G. Rajaraman, *J. Am. Chem. Soc.*, 2013, **135**, 4235-4249.
50. S.-P. Huang, Y. Shiota and K. Yoshizawa, *Dalton Trans.*, 2013, **42**, 1011-1023.
51. T. Saito, Y. Kataoka, Y. Nakanishi, Y. Kitagawa, T. Kawakami, S. Yamanaka, M. Okumura and K. Yamaguchi, *Supramol. Chem.*, 2010, **23**, 83-87.
52. M. J. Frisch, G. W. Trucks, H. B. Schlegel, G. E. Scuseria, M. A. Robb, J. R. Cheeseman, G. Scalmani, V. Barone, B. Mennucci, G. A. Petersson, H. Nakatsuji, M. Caricato, X. Li, H. P. Hratchian, A. F. Izmaylov, J. Bloino, G. Zheng, J. L. Sonnenberg, M. Hada, M. Ehara, K. Toyota, R. Fukuda, J. Hasegawa, M. Ishida, T. Nakajima, Y. Honda, O. Kitao, H. Nakai, T. Vreven, J. A. Montgomery, J. E. Peralta, F. Ogliaro, M. Bearpark, J. J. Heyd, E. Brothers, K. N. Kudin, V. N. Staroverov, R. Kobayashi, J. Normand, K. Raghavachari, A. Rendell, J. C. Burant, S. S. Iyengar, J. Tomasi, M. Cossi, N. Rega, J. M. Millam, M. Klene, J. E. Knox, J. B. Cross, V. Bakken, C. Adamo, J. Jaramillo, R. Gomperts, R. E. Stratmann, O. Yazyev, A. J. Austin, R. Cammi, C. Pomelli, J. W. Ochterski, R. L. Martin, K. Morokuma, V. G. Zakrzewski, G. A. Voth, P. Salvador, J. J. Dannenberg, S. Dapprich, A. D. Daniels, Farkas, J. B. Foresman, J. V. Ortiz, J. Cioslowski and D. J. Fox, Wallingford CT, 2009.
53. F. Neese, *WIRES*, 2012, **2**, 73-78.
54. S. Grimme, *J. Comput. Chem.*, 2006, **27**, 1787-1799.
55. A. Pabis, I. Geronimo and P. Paneth, *J. Phys. Chem. B*, 2014, **118**, 3245-3256.
56. P. J. Hay and W. R. Wadt, *J. Chem. Phys.*, 1985, **82**, 270-283.
57. P. J. Hay and W. R. Wadt, *J. Chem. Phys.*, 1985, **82**, 299-310.
58. R. Ditchfield, W. J. Hehre and J. A. Pople, *J. Chem. Phys.*, 1971, **54**, 724-728.
59. A. Schäfer, H. Horn and R. Ahlrichs, *J. Chem. Phys.*, 1992, **97**, 2571-2577.
60. A. Schäfer, C. Huber and R. Ahlrichs, *J. Chem. Phys.*, 1994, **100**, 5829-5835.
61. G. A. Zhurko, *ChemCraft software, version 1.6*, 2014.
62. J. Tomasi, B. Mennucci and R. Cammi, *Chem. Rev.*, 2005, **105**, 2999-3094.
63. L. Noodleman, *J. Chem. Phys.*, 1981, **74**, 5737-5743.
64. L. Noodleman and E. R. Davidson, *Chem. Phys.*, 1986, **109**, 131-143.
65. E. J. B. a. J. G. S. E. van Lenthe, *J. Chem. Phys.*, 1993, **99**, 4597-4610.
66. C. J. v. Wullen, *Chem. Phys.*, 1998, **109**, 392-399.
67. M. Radoul, M. Sundararajan, A. Potapov, C. Riplinger, F. Neese and D. Goldfarb, *Phys, Chem. Chem. Phys.*, 2010, **12**, 7276-7289.
68. F. Neese, *Inorg. Chim. Acta*, 2002, **337**, 181-192.
69. G. Rajaraman, E. Ruiz, J. Cano and S. Alvarez, *Chem. Phys. Lett.*, 2005, **415**, 6-9.
70. S. Tewary, I. A. Gass, K. S. Murray and G. Rajaraman, *Eur. J. Inorg. Chem.*, 2013, **2013**, 1024-1032.
71. N. Berg, T. Rajeshkumar, S. M. Taylor, E. K. Brechin, G. Rajaraman, L. F. Jones, N. Berg, T. Rajeshkumar, S. M. Taylor, E. K. Brechin, G. Rajaraman and L. F. Jones, *Chem. Eur. J.*, 2012, **18**, 5906-5918.
72. P. Jayapal and G. Rajaraman, *Phys. Chem. Chem. Phys.*, 2012, **14**, 9050-9053.
73. S. K. Singh, N. K. Tibrewal and G. Rajaraman, *Dalton Trans.*, 2011, **40**, 10897-10906.
74. G. Rajaraman, M. Murugesu, E. C. Sañudo, M. Soler, W. Wernsdorfer, M. Helliwell, C. Muryn, J. Raftery, S. J. Teat, G. Christou and E. K. Brechin, *J. Am. Chem. Soc.*, 2004, **126**, 15445-15457.
75. P. Christian, G. Rajaraman, A. Harrison, J. J. W. McDouall, J. T. Raftery and R. E. P. Winpenny, *Dalton Trans.*, 2004, 1511-1512.
76. D. Gatteschi and A.Bencini, *EPR of Exchange Coupled Systems*, Springer-Verlag, Berlin 1990.
77. Note here that since geometry optimization was not successful for this spin state, single point calculations on $^{6}2_{(is,is)}$ geometry was utilized to compute the energy
78. J. T. Groves, R. C. Haushalter, M. Nakamura, T. E. Nemo and B. J. Evans, *J. Am. Chem. Soc.*, 1981, **103**, 2884-2886.
79. S. R. Bell and J. T. Groves, *J. Am. Chem. Soc.*, 2009, **131**, 9640-9641.
80. S. Shaik, D. Kumar, S. P. de Visser, A. Altun and W. Thiel, *Chem. Rev.*, 2005, **105**, 2279-2328.
81. K.-B. Cho, X. Wu, Y.-M. Lee, Y. H. Kwon, S. Shaik and W. Nam, *J. Am. Chem. Soc.*, 2012, **134**, 20222-20225.
82. F. Ogliaro, N. Harris, S. Cohen, M. Filatov, S. P. de Visser and S. Shaik, *J. Am. Chem. Soc.*, 2000, **122**, 8977-8989.
83. J. N. Harvey and M. Aschi, *Faraday Discuss.*, 2003, **124**, 129-143.
84. P. Barman, A. K. Vardhaman, B. Martin, S. J. Wörner, C. V. Sastri and P. Comba, *Angew. Chem. Int. Ed.*, 2015, **54**, 2095-2099.
85. S. Ye and F. Neese, *Proc. Nat. Acad. Sci.*, USA, 2011, **108**, 1228-1233.
86. G. Schwarz, R. R. Mendel and M. W. Ribbe, *Nature*, 2009, **460**, 839-847.
87. M. Filatov, N. Harris and S. Shaik, *Angew. Chem. Int. Ed.*, 1999, **38**, 3510-3512.
88. S. Shaik, S. P. de Visser, F. Ogliaro, H. Schwarz and D. Schröder, *Curr. Opin. Chem. Biol.*, 2002, **6**, 556-567.

TOC:

Methane activation by dinuclear high-valent iron-oxo species: Do we need two metals to activate such inert bonds?

Our theoretical study using DFT methods where electronic structure details and mechanistic aspects are established answer this intriguing question.